Geophysical Journal International

*Geophys. J. Int.* (2016) **204,** 544–554 doi: 10.1093/gji/ggv465
GJI Seismology

# Temporal stress changes associated with the 2008 May 29 $M_W$ 6 earthquake doublet in the western South Iceland Seismic Zone

Martin Hensch,[1,*] Björn Lund,[2] Thóra Árnadóttir[1] and Bryndís Brandsdóttir[3]

[1]*Nordic Volcanological Center, Institute of Earth Sciences, University of Iceland, Reykjavik, Iceland. E-mail: martin@vedur.is*
[2]*Department of Earth Sciences, Uppsala University, Uppsala, Sweden*
[3]*Institute of Earth Sciences, University of Iceland, Reykjavik, Iceland*

Accepted 2015 October 23. Received 2015 October 22; in original form 2015 June 29

## SUMMARY

On 2008 May 29, two magnitude $M_W \sim 6$ earthquakes occurred on two adjacent N-S faults in the western South Iceland Seismic Zone. The first main shock was followed approximately 3 s later by the rupture on a parallel fault, about 5 km to the west. An intense aftershock sequence was mostly confined to the western fault and an E-W aligned zone, extending west of the main shock region into the Reykjanes oblique rift. In this study, a total of 325 well-constrained focal mechanisms were obtained using data from the permanent Icelandic SIL seismic network and a temporary network promptly installed in the source region following the main shocks, which allowed a high-resolution stress inversion in short time intervals during the aftershock period. More than 800 additional focal mechanisms for the time period 2001–2009, obtained from the permanent SIL network, were analysed to study stress changes associated with the main shocks. Results reveal a coseismic counter-clockwise rotation of the maximum horizontal stress of 11 $\pm$ 10° (95 per cent confidence level) in the main rupture region. From previous fault models obtained by inversion of geodetic data, we estimate a stress drop of about half of the background shear stress on the western fault. With a stress drop of 8–10 MPa, the pre-event shear stress is estimated to 16–20 MPa. The apparent weakness of the western fault may be caused by fault properties, pore fluid pressure and the vicinity of the fault to the western rift zone, but may also be due to the dynamic stress increase on the western fault by the rupture on the eastern fault. Further, a coseismic change of the stress regime—from normal faulting to strike-slip faulting—was observed at the northern end of the western fault. This change could be caused by stress heterogeneities, but may also be due to a southward shift in the location of the aftershocks as compared to prior events.

**Key words:** Earthquake source observations; Seismicity and tectonics; Oceanic transform and fracture zone processes.

## 1 INTRODUCTION

Major earthquakes can significantly impact the stress field in close vicinity of the rupture. Significant rotation of the causative stress field has been observed for a number of earthquakes in southern California, for example, the $M_W$ 7.3 Landers earthquake 1992 (Hauksson 1994; Hardebeck & Hauksson 2001a), for the $M_W$ 7.4 Izmit (Turkey) earthquake in 1999 (Ickrath *et al.* 2013), as well as for several subduction zone earthquakes, such as the $M_W$ 9.0 Tohoku earthquake offshore Japan 2011 and the $M_W$8.8 Maule earthquake in Chile 2010 (Hasegawa *et al.* 2011; Hardebeck 2012). Changes in the stress orientation as a response to major earthquakes can give a measure of the magnitude of the differential stress at seismogenic depth, as the rotation angle depends on the orientation of the fault relative to the pre-event stress field and the ratio of the earthquake stress drop to the background differential stress level (Hardebeck & Hauksson 2001a).

The target area of this study is the Ölfus region in the western part of the South Iceland Seismic Zone (SISZ), which was struck by two $M_W$ 6 earthquakes within three seconds on 2008 May 29 at 15:45 UTC (Hreinsdóttir *et al.* 2009; Decriem *et al.* 2010; Brandsdóttir *et al.* 2010). The SISZ is an approximately 80 km wide left-lateral E–W transform zone, bridging the offset between the Eastern Volcanic Zone and the Hengill triple junction (Fig. 1). The regional driving force of plate movements in South Iceland is the spreading of the North American and Eurasian plates, in the approximate direction of 101° in South Iceland (DeMets *et al.* 2010). In the brittle crust, plate motion in the SISZ is accommodated by several

*Now at: Icelandic Meteorological Office, Bústaðavegur 7-9, 108 Reykjavik, Iceland.

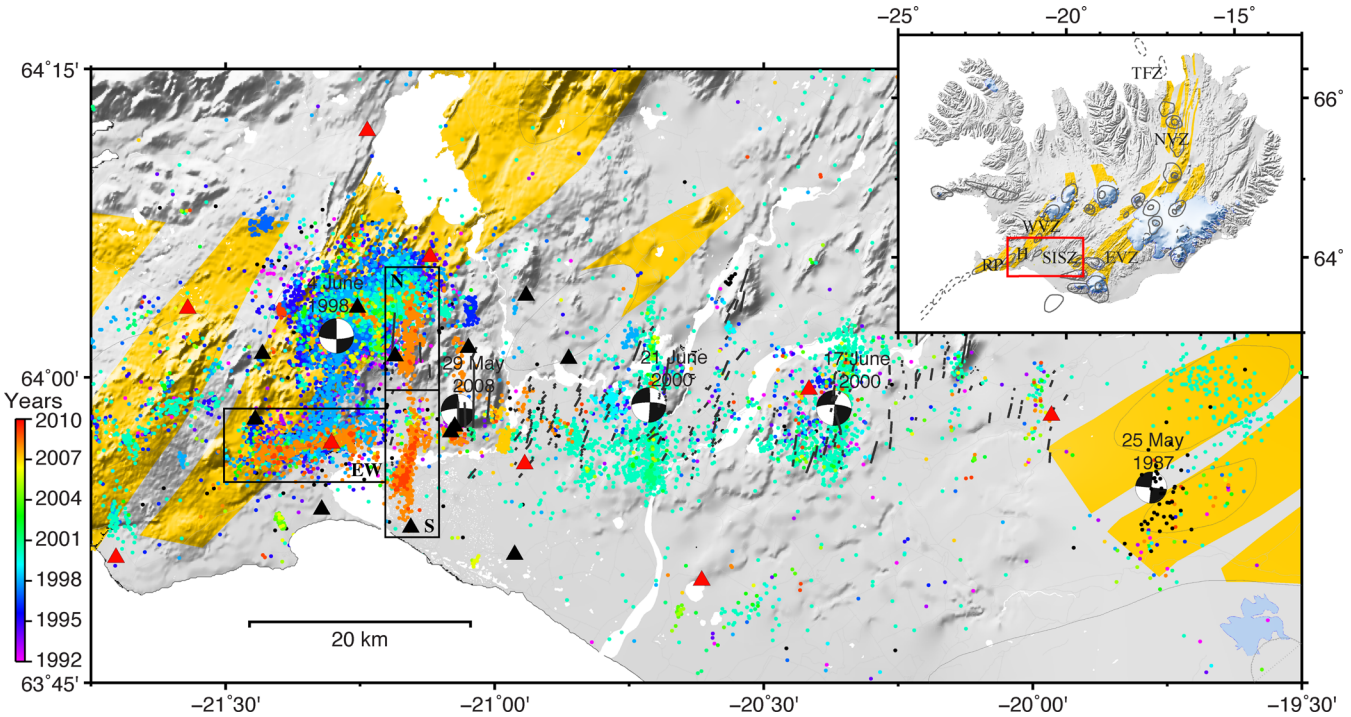


**Figure 1.** A map of the South Iceland Seismic Zone (SISZ), outlined with a red box on the tectonic map of Iceland (upper right), based on (Einarsson & Sæmundsson 1987). Fissure swarms within the volcanic zones are yellow: Reykjanes Peninsula (RPRZ), Hengill central volcano (H), Western Volcanic Zone (WVZ), Eastern Volcanic Zone (EVZ) and Northern Volcanic Zone (NVZ). Beachballs indicate focal mechanisms of major events within the recent earthquake sequence (CMT catalogue) and dots mark event locations from the SIL database (IMO), colour-coded by time. Red triangles show seismic stations of the permanent SIL network, black triangles temporary seismometers. The 2008 rupture planes and an E-W aligned region of aftershocks are highlighted with orange and red dots in the western part of the SISZ. The three main aftershock clusters are outlined with black boxes (Table 1). Dark grey lines show strike-slip surface faults mapped by Einarsson (2010).

N-S trending right-lateral strike-slip faults spaced approximately 2–5 km apart (Einarsson *et al.* 1981). Hence, the SISZ differs from other transform zones along the Mid-Atlantic ridge plate boundary, with strike-slip fault orientations that are almost perpendicular to the direction of plate motion. Geodetic studies suggest that the N-S faults are loaded by E-W shear below a locking depth of approximately 10–20 km (Árnadóttir *et al.* 2006). The seismically active region within the SISZ is approximately 10 km wide in north–south direction, with seismogenic depth increasing eastwards (Stefánsson *et al.* 1993; Bjarnason *et al.* 1993). Aftershocks of the latest large events in the SISZ clustered between 6 and 13 km depth for the 1987 Vatnafjöll event (Bjarnason & Einarsson 1991) and between the surface and about 10 km depth for the 2000 June 17 and 21 events (Hjaltadóttir & Vogfjörd 2005; Hjaltadóttir 2009). Aftershocks of the 2008 May earthquake rarely exceeded 8 km depth (Brandsdóttir *et al.* 2010).

The 2008 May earthquakes are part of a major sequence of $M > 5$ earthquakes. Comparable sequences have occurred repeatedly in the SISZ since the settlement in Iceland, separated by relatively quiet periods of 45–112 yr (Einarsson & Björnsson 1979). The durations of these sequences range between days and years, usually starting with a large event in the eastern part of the SISZ followed by events to the west, of smaller or equal magnitude. The previous major sequence started in 1896 with five events of magnitude $M_S$ 6–6.9 within two weeks. The $M_S$ 7 event in 1912 in the eastern part of the SISZ is one of few examples of single earthquakes that are not assigned to a specific sequence (Einarsson *et al.* 1981).

The current sequence started in 1987 May with a $M_S$ 5.8 earthquake in the transition zone between the eastern SISZ and the Eastern Volcanic Zone (Bjarnason & Einarsson 1991), continuing on 2000 June 17 and 21 with two $M_W \sim 6.5$ earthquakes in the central SISZ (Árnadóttir *et al.* 2001; Pedersen *et al.* 2003; Hjaltadóttir 2009). The 2008 May events occurred during a span of about three seconds, on two adjacent faults 4–5 km apart, close to the Hengill triple junction (Hreinsdóttir *et al.* 2009). Being first reported as a single event with a composite magnitude of $M_W$ 6.3 (Global CMT), detailed geodetic studies of the coseismic surface deformation revealed two main shocks with moment magnitudes ranging from $M_W$ 5.8 to $M_W$ 6 (Hreinsdóttir *et al.* 2009; Decriem *et al.* 2010).

The short time interval between the two main shocks of about three seconds suggests dynamic triggering of the second rupture (Kross fault) by surface waves from the first (Ingólfsfjall fault) (Hreinsdóttir *et al.* 2009). The activation of an east–west aligned segment west of the main shock region (Figs 1 and 2) is likely to have been statically triggered by an increase of Coulomb failure stress (Decriem *et al.* 2010). Comparable induced stress changes on adjacent faults have been suggested for a number of earthquakes including the SISZ 2000 earthquakes (Árnadóttir *et al.* 2003) as well as the 1992 Landers $M_W$ 7.3 earthquake (Harris & Simpson 1992).

The aim of this study is to derive high-resolution stress field orientations based on well-constrained focal mechanism data prior to and following the 2008 May main shocks. Spatial and temporal partitioning of the data facilitates the analysis of temporal changes of the local stress field in the 2008 May epicentral area as a response to the main ruptures. We use data from the permanent Icelandic SIL seismic network and a temporary network that was promptly installed in the first days of the aftershock sequence and operated

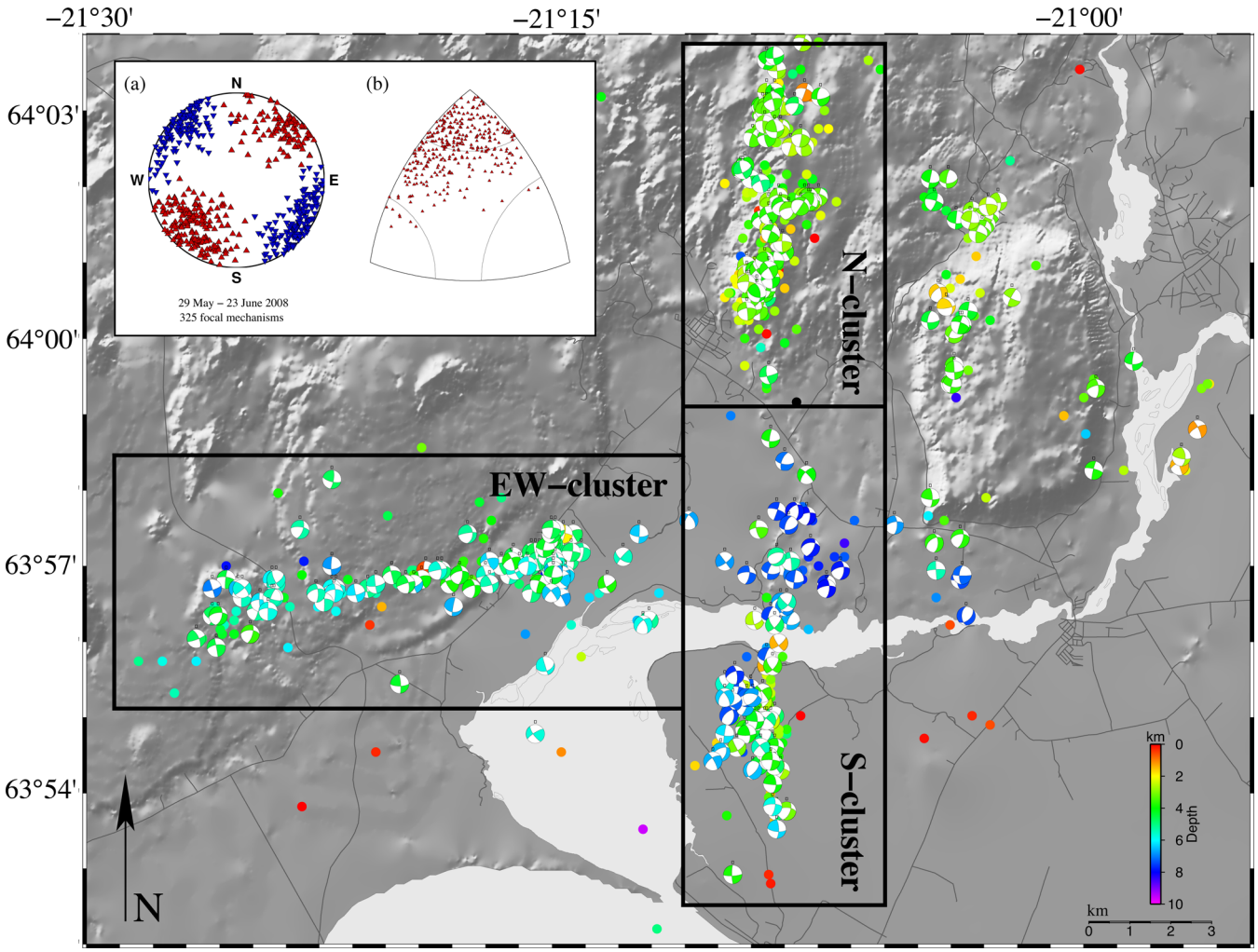


**Figure 2.** Focal mechanisms obtained using FOCMEC, together with all SEISAN locations of the 2008 sequence, colour-coded with respect to depth. Black boxes mark the outlines of the three defined earthquake clusters. The box in the upper left shows: (a) summary plot of *P*- (red triangles) and *T*-axes (blue triangles) of 325 focal mechanisms. (b) Faulting regimes after Kagan (2005).

for about four weeks (Brandsdóttir *et al.* 2010). This study covers the years from 2001 until end of 2009, whereof the time between 2008 May 29 until June 23 makes use of the temporary network data.

Three prominent clusters of high aftershock activity were identified and analysed in this study (Figs 1 and 2). Two clusters are confined to the western Kross fault (here after referred to as N-cluster and S-cluster, see Fig. 2). Slip models determined from inversion of geodetic data indicate maximum slip during the main event in the northern part of the S-cluster (Hreinsdóttir *et al.* 2009; Decriem *et al.* 2010). The third cluster covers the E-W elongated zone west of the main shock region (EW-cluster). No significant slip was identified in the EW-cluster from geodetic studies (Decriem *et al.* 2010). Aftershock activity on the eastern Ingólfsfjall fault was low compared to the Kross fault. The lack of aftershocks on this fault might have been caused by stress changes due to the subsequent rupture on the adjacent Kross fault. Further, activity prior to the main shocks was located on the southern part of the Ingólfsfjall fault, while a few aftershocks clustered on the northern part. In contrast, activity on the Kross fault was rather evenly distributed prior to and after the main shocks. Detailed analyses of the stress field with respect to time were thus not possible for the Ingólfsfjall fault.

## 2 SEISMIC DATA

Following the 2008 main shocks, 11 temporary seismic stations (Lennartz LE-3D 5sec, RefTek RT130 digitizers) were installed in the next three days in order to densify the permanent SIL seismic network in the epicentral area (Brandsdóttir *et al.* (2010) and Fig. 1). The SIL network is run by the Icelandic Meteorological Office (IMO; Bödvarsson *et al.* 1999). The magnitude of completeness in the SISZ is around $M_L$ 0 (Wyss & Stefánsson 2006). Horizontal location uncertainties of the permanent SIL network in the target region are comparable to the temporary network (∼1 km), but depth uncertainties due to fewer sensors in the epicentral region might affect the subsequent determination of focal mechanisms for smaller events.

The purpose of the temporary network was to close potential azimuthal gaps, to improve estimates of event depths using near zero-offset stations and to better constrain focal mechanisms of small events. Although the detection level of the seismic networks, in particular the temporary stations, was affected by weather and human noise, an automatic detection routine located nearly 20 000 aftershocks throughout June using the permanent and temporary stations (Brandsdóttir *et al.* 2010).

In this study, SEISAN 8.2.1 (Havskov & Ottemöller 2008) was used to set up a joint database of the permanent and temporary network data. Based on the IMO list of automatically detected events, 650 events with $M_L > 1.0$ were manually repicked and relocated. The SIL velocity model (Stefánsson *et al.* 1993) was used to locate the events. Earthquake depth uncertainties within the joint network are around 1 km, horizontal uncertainties are in the range of 0.5–1 km. The centre of gravity of event locations in the S-cluster is stable within ±1 km over the whole pre- and aftershock period. Largest deviations of the cluster centroid over time are found for the N-cluster, where events move southwards by about 3 km following the main shock, as well as for the EW-cluster, where events move eastwards and upwards by about 2 km, respectively. The stability of cluster centroids is crucial for the following stress analysis, as stress homogeneity within each cluster is assumed. Any offset in the event location might cause apparent changes of the maximum horizontal stress direction $\mathbf{S}_H$, as shown by Townend & Zoback (2001) for the Landers earthquake. The observation of a real rotation of the $\mathbf{S}_H$ azimuth requires activity in the same location before and after the main shock, which is apparent for the S-cluster, but might be disputed for the N- and EW-clusters, albeit the centre of gravity is well within the average extent of each of the three clusters.

### 2.1 Focal mechanisms

A total of 325 well-constrained focal mechanisms were derived using the joint seismic network in the period 2008 May 29–June 23. The mechanisms were obtained using the algorithm FOCMEC (Snoke *et al.* 1984), which calculates double-couple focal mechanisms based on *P*-wave polarities and P/SV amplitude ratios. *P*-wave polarities were determined during manual picking of arrival times in SEISAN. Including amplitude ratios did neither improve nor significantly affect the focal mechanism estimates and was thus omitted for most events. The threshold for the minimum number of well-constrained *P*-wave polarities was set to 8 and polarity misfits were not allowed. The uncertainty of the focal mechanism estimates ranges around 3–10°, as the dense seismic network allowed us to constrain mechanisms quite well even for small events with only 8 polarity readings. The maximum number of used *P* polarities is 21, the vast majority of events have 12–15 polarity readings. In addition, approximately 550 pre-main shock focal mechanisms for the period 2001 January 1 until 2008 May 29 and around 330 mechanisms during 2008 June 24 and 2009 December 31, after the temporary network was dismantled, were obtained using the sparser permanent SIL network. The SIL software calculates best-fitting mechanism solutions based on *P* polarities and P, SV and SH amplitudes (Slunga 1981; Rögnvaldsson & Slunga 1993). For this study, focal mechanisms with at least three polarity readings and eight stations with amplitude information were selected. The mean magnitude of events fulfilling these quality criteria is $M_L$ 1. In order to obtain a sufficient number of focal mechanisms for reliable stress inversion results, the epicentral zone was divided into three areas (Figs 1 and 2). Coordinates of the boxes outlining the three clusters are given in Table 1.

**Table 1.** Coordinates of aftershock clusters shown in Fig. 2.

| Cluster | Latitude [°N] | Longitude [°W] |
|---|---|---|
| N | 63.99−64.09 | 21.20−21.10 |
| S | 63.87−63.99 | 21.20−21.10 |
| EW | 63.915−63.975 | 21.50−21.20 |

The vast majority of derived focal mechanisms show strike-slip faulting with a NE–SW pressure axis and a NW–SE tension axis (Fig. 2). Slight normal faulting components were found for a few events in all clusters, especially in the N-cluster. Aftershocks in the N- and S-clusters on the main rupture planes or on close-by faults show dominantly right-lateral strike-slip faulting. For the EW-cluster, the event distribution might suggest left-lateral strike-slip motion on an E-W fault, however right-lateral motion on a series of N-S oriented faults, or a mixture of both, has been previously proposed in various studies based on relative relocations (Rögnvaldsson *et al.* 1998a,b; Vogfjörd *et al.* 2005).

## 3 STRESS INVERSION

The causative stress tensor was calculated by inverting the focal mechanism data using the method of Lund & Slunga (1999). The algorithm is based on a grid search inversion scheme by Gephart & Forsyth (1984) with the addition of fault plane selection based on a stability criterion. The method estimates a stress tensor in form of the directions of its three principle stress axes $\sigma_1$, $\sigma_2$ and $\sigma_3$, as well as the relative magnitude of $\sigma_2$, given by $R = (\sigma_1 - \sigma_2)/(\sigma_1 - \sigma_3)$. Although absolute magnitudes of the stresses can not be calculated from focal mechanisms only, this approach allows the determination of the direction of the maximum horizontal stress $\mathbf{S}_H$ (Lund & Townend 2007). The method further provides confidence limits for the calculated parameters and the preferred nodal planes. The parameter space is searched using 5° steps for the orientations of the stress axes and 0.1 steps for $R$ in the grid search. The orientation of $\mathbf{S}_H$ is calculated as the circular average of all possible $\mathbf{S}_H$ directions within 95 per cent confidence levels. An example is given in Fig. 3, showing the stress tensor inversion results for the 325 aftershock focal mechanisms from the temporary seismic network deployment (2008 May 29–June 23). The solution reflects an average strike-slip regime with a maximum horizontal stress direction of 32±6°, a minimum horizontal stress direction of 122 ± 8° and $R = 0.6 \pm 0.1$ for the whole aftershock region. The 95 per cent confidence of the inversion is in the range of the focal mechanism uncertainty of 3–10° and better than the accuracy of the more poorly constrained focal mechanisms.

For comparison we also used the stress inversion technique by Dahm and Plenefisch (personal communication, 2009 and Reinhardt 2007) for the 325 aftershocks, which revealed comparable results for the stress axes directions, but a slightly lower $R$ of 0.4 ± 0.1. In a strike-slip regime, $R < 0.5$ indicates slight tendencies toward normal faulting, while values $R > 0.5$ indicate slight reverse components. As our $R$-values are close to 0.5 we find a stable strike-slip regime. Table 2 summarizes results from the inversion of all 325 aftershock focal mechanisms. The strike directions of maximum and minimum stress axes, $\sigma_1$ and $\sigma_3$, determined by the two different inversion algorithms differ by 4–5°, and are within the uncertainties of each other. The minimum horizontal stress direction using the Lund & Slunga (1999) inversion method (N122 ± 8°E) is comparable to the average minimum stress direction in the Ölfus area (N120°E, Lund & Slunga 1999) and on the Reykjanes peninsula west of Ölfus (N120 ± 6°E), determined by Keiding *et al.* (2009). The overall spreading direction across south Iceland predicted by the MORVEL plate motion model is ∼101° (DeMets *et al.* 2010), about 20° off the minimum stress direction observed in the target region in this and previous studies in South Iceland.

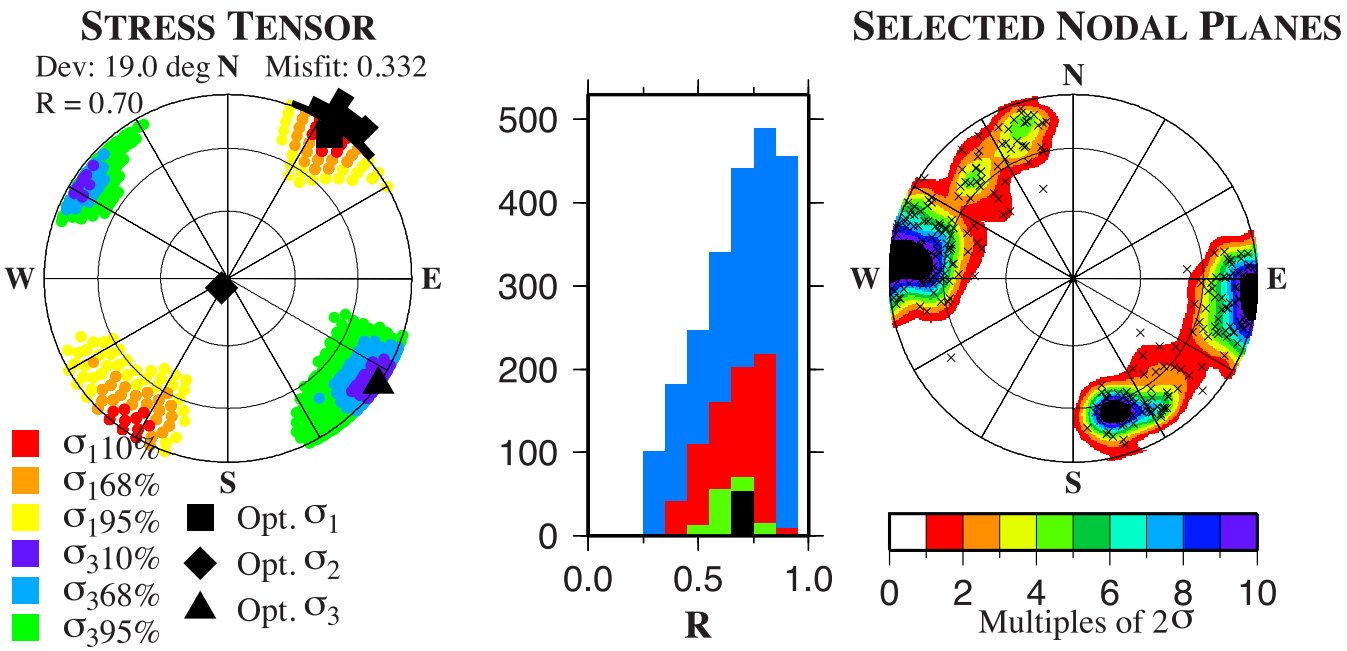


**Figure 3.** Stress tensor estimation for all 325 focal mechanisms between 2008 May 29 and June 23 in the Ölfus region. The stress tensor is represented in an equal area lower hemisphere projection of the principle stress directions. Stress axes are indicated with the following symbols: $\sigma_1$ (square), $\sigma_2$ (diamond) and $\sigma_3$ (triangle). Warm colours represent the confidence regions of $\sigma_1$, cold colours for $\sigma_3$. The histogram on the outer sphere gives the maximum horizontal stress direction for all stress tensors within the 95 per cent confidence level. The histogram in the middle of the plot shows the best fit for $R$ (black) and its confidence regions 95 per cent (blue), 68 per cent (red) and 10 per cent (green). To the right is an equal area projection of Kamb contours of the poles to the selected nodal planes.

**Table 2.** Azimuth (az.) and plunge (pl.) angles obtained with stress inversion methods ([1] Lund & Slunga (1999) and [2] Dahm and Plenefisch, personal communication, 2009). The overall spreading direction predicted from the MORVEL plate motion model is given for comparison ([3] DeMets *et al.* 2010). Reported uncertainties are at the 95 per cent confidence level.

| | Az. $\sigma_1$[°] | Pl. $\sigma_1$[°] | Az. $\sigma_3$[°] | Pl. $\sigma_3$[°] | $R = \frac{\sigma_1-\sigma_2}{\sigma_1-\sigma_3}$ |
|---|---|---|---|---|---|
| 1 | 32 ± 6 | 10 ± 6 | 122 ± 8 | 5 ± 8 | 0.6 ± 0.1 |
| 2 | 37 ± 10 | 21 ± 10 | 126 ± 10 | 4 ± 10 | 0.4 ± 0.1 |
| 3 | – | – | 101 | – | – |

### 3.1 Temporal partitioning of the events

Stress inversions of focal mechanisms within each earthquake cluster were temporally subdivided into three periods, 2001 January–2008 May 28, 2008 May 29–June 23 and 2008 June 24–2009 December (Table 3). Inversion results for the pre-event period reveal a maximum horizontal stress $\mathbf{S}_H$ of 54 ± 6° within the N-cluster. Further, the stress regime in the N-cluster changed from normal to strike-slip faulting in response to the earthquakes (Fig. 4). Stress results for the third time interval suggest a change back to normal faulting. However, pre- and aftershock activity within the N-cluster are spatially slightly offset, which might reflect activity on normal faults within the western rift prior to the main events, which originated on strike-slip faults within the SISZ. No systematic change of the orientation of $\mathbf{S}_H$ is observed in the N-cluster. The pre-main shock orientation of $\mathbf{S}_H$ in the S-cluster is 36 ± 5° and a stable counter-clockwise coseismic rotation of $\mathbf{S}_H$ of 11 ± 10°, from 36 ± 5° to 25 ± 5°, is observed within this cluster. The $\mathbf{S}_H$ direction in the EW-cluster prior to the main shocks is 36 ± 8° and no systematic change of the $\mathbf{S}_H$ direction is observed in this cluster. Variations in the $\mathbf{S}_H$ orientations are within the 95 per cent confidence level for all three time intervals.

Investigating short-term stress changes associated with the main shocks requires further temporal partitioning of each cluster. We therefore split the pre-main shock period into two year intervals (2001–2002, ..., 2007–2008 May 28) and the aftershock sequence into as short intervals as possible, depending on the availability of focal mechanisms. For the period of the temporary network we chose intervals of 3–10 d, with a minimum of 25 focal mechanisms in each interval.

All values of $\mathbf{S}_H$ within the S-cluster decreased from >30° in 2001–2008 May to <30° following the main shocks. They were highest (37 ± 6°) in 2005–2006 and lowest (25 ± 6°) during the first three days after the main shocks. We note that finer temporal partitioning increases uncertainties in the inversion results such that the uncertainty levels now overlap. Between the last pre- and first post-event interval, the orientation of $\mathbf{S}_H$ rotated counter-clockwise from 35 ± 6° to 25 ± 6°. The rotation of $\mathbf{S}_H$ appears stable throughout the whole aftershock sequence (Fig. 5b). Summarizing, the observed stress rotation on the southern Kross fault is 11 ± 10° at the 95 per cent confidence limit between the average pre- and post-main shock period. The rotation between the last interval prior to, and the first interval following the main shocks is 10 ± 12° at the 95 per cent confidence limit.

**Table 3.** Average orientations of $\mathbf{S}_H$ of all three clusters for the pre-event interval (2001 January 1–2008 May 28), the operation time of the temporary network (2008 May 29 –2008 June 23) and the post-event interval following the temporary network (2008 June 24–2009 December 31).

| | SHmax[°] | | |
|---|---|---|---|
| Cluster | Pre-event | Temporary network | Post-event |
| N | 54 ± 6 | 53 ± 6 | 54 ± 6 |
| S | 36 ± 5 | 25 ± 5 | 27 ± 6 |
| EW | 36 ± 8 | 35 ± 8 | 40 ± 6 |

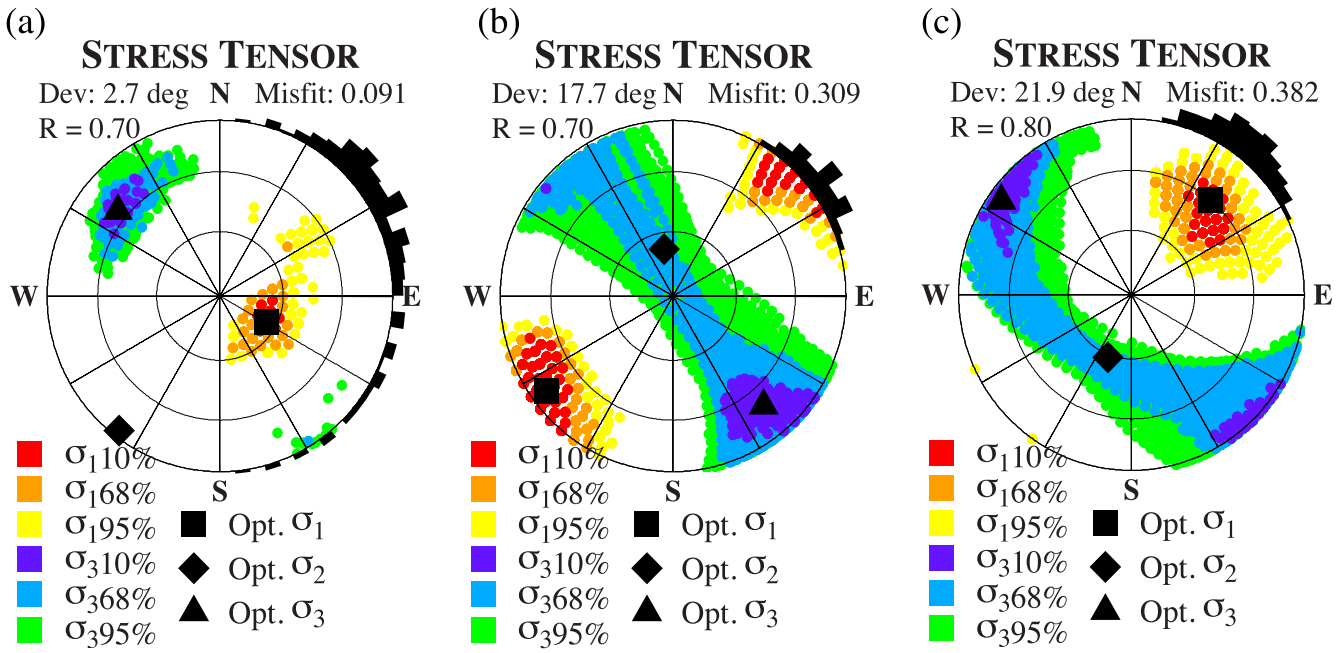


**Figure 4.** Stress inversion results (stress orientations and confidence levels) for the northern cluster in three investigated time windows, (a) 2001 January 1 until 2008 May 29 (167 focal mechanisms), (b) 2008 May 29 until June 24 (84 mechanisms) and (c) 2008 June 24 until 2009 December 31 (109 mechanisms). Symbols and colours are the same as in Fig. 3.

No systematic variation in the orientation of $\mathbf{S}_H$ occurred in the N- and EW- clusters (Figs 5a and c). Large fluctuations between 59 $\pm$ 5° and 48 $\pm$ 5° were found within the N-cluster for the period between 2001 and 2009, as well as 41 $\pm$ 5° and 29 $\pm$ 7° for the EW-cluster. A minor clockwise rotation of $\mathbf{S}_H$ for the EW-cluster during the first three days of the aftershock sequence is instantly compensated during the next time interval. A clockwise rotation of $\mathbf{S}_H$ from a pre-main shock stress angle $\Theta$<45° would imply a stress load. But relatively high residuals in all time intervals for both the N- and EW-clusters do not allow any conclusion on stress rotations related to the main shocks.

## 4 DISCUSSION

A maximum horizontal stress direction of N30°E $\pm$ 6° observed for both the Reykjanes peninsula (Keiding *et al.* 2009) and the Ölfus region (Lund & Slunga 1999), is consistent with our findings for the S- and EW-clusters. The average 54 $\pm$ 6° found for the northern cluster are within the range of $\mathbf{S}_H$ directions found for the whole SISZ (Stefánsson *et al.* 1993).

The only significant change in the horizontal stress orientation related to the 2008 May earthquake doublet was observed in the S-cluster, which is the location of maximum slip based on models of coseismic surface deformation (Hreinsdóttir *et al.* 2009; Decriem *et al.* 2010). All values for $\mathbf{S}_H$ were consistently found >30° before and <30° after the main rupture in the S-cluster. The rotation of $\mathbf{S}_H$ of 11 $\pm$ 10° between its average orientation prior to and after the main shocks is just above the limit of statistical significance for 95 per cent uncertainty levels. A slight overlap in rotation uncertainties of 10 $\pm$ 12° is observed between the last pre- and first post-main shock interval. However, Hardebeck & Hauksson (2001b) showed that the grid search method we use (Gephart & Forsyth 1984) is generally more accurate for high-quality data, but tends to overestimate uncertainties and that the 68 per cent confidence level of Gephart & Forsyth (1984) corresponds to 80 per cent confidence of the linear inversion method of Michael (1984, 1987), which is commonly used in literature (e.g. Hardebeck & Hauksson 2001b). Using 68 per cent confidence decreases the uncertainty and the rotation of $\mathbf{S}_H$ between its average pre- and post-event rotation is then 11 $\pm$ 6°.

The counter-clockwise rotation found in the S-cluster is illustrated in Fig. 6. Based on these values, the ratio of the earthquake stress drop to the background maximum shear stress ($\Delta\tau/\tau$) can be calculated following Hardebeck & Hauksson (2001a):

$$\tan(\Delta\Theta) = \frac{1 - \frac{\Delta\tau}{\tau}\sin 2\Theta - \sqrt{\left(\frac{\Delta\tau}{\tau}\right)^2 + 1 - 2\frac{\Delta\tau}{\tau}\sin 2\Theta}}{\frac{\Delta\tau}{\tau}\cos 2\Theta} \quad (1)$$

where $\Theta$ is the angle between the fault and the pre-earthquake maximum stress direction and $\Delta\Theta$ the observed rotation angle. Fig. 7 shows our observed stress rotation $\Delta\Theta$ for different ratios of shear stress change $\Delta\tau/\tau$ with respect to $\Theta$. Using the strike angle of the southern fault segment, N3°E (Decriem *et al.* 2010), we find that $\Delta\tau/\tau$ is 0.5 (0.1–0.7) for the rotation between the pre- and post-main shock averages and 0.5 (−0.1–0.8) for the direct rotation between the last pre- and first post-main shock intervals. Numbers in brackets give the range of $\Delta\tau/\tau$ and are based on minimum and maximum rotation within the 95 per cent confidence levels of $\mathbf{S}_H$.

As there are no studies of the stress drop in the main event, we estimate $\Delta\tau$ using two different approaches. According to Brune (1970, 1971), the stress drop on a circular crack can be approximated using the seismic moment $M_0$ and the *S*-wave corner frequency $f_0$ with

$$\Delta\tau = \frac{7}{16} M_0 \left(\frac{2\pi f_0}{2.34\beta}\right)^3 \quad (2)$$

The shear wave velocity $\beta$ was assumed to be 3500 m s$^{-1}$, the corner frequency $f_0$ was found at 0.35 $\pm$ 0.025 Hz using broad-band seismometer data of the permanent SIL network. The seismic moment $M_0$ of the main shock on the Kross fault ($M_W$=5.9; Decriem *et al.* (2010)) is $1.2\times10^{18}$ Nm. From these assumptions, the stress drop $\Delta\tau$ is estimated to be 10 $\pm$ 2 MPa.

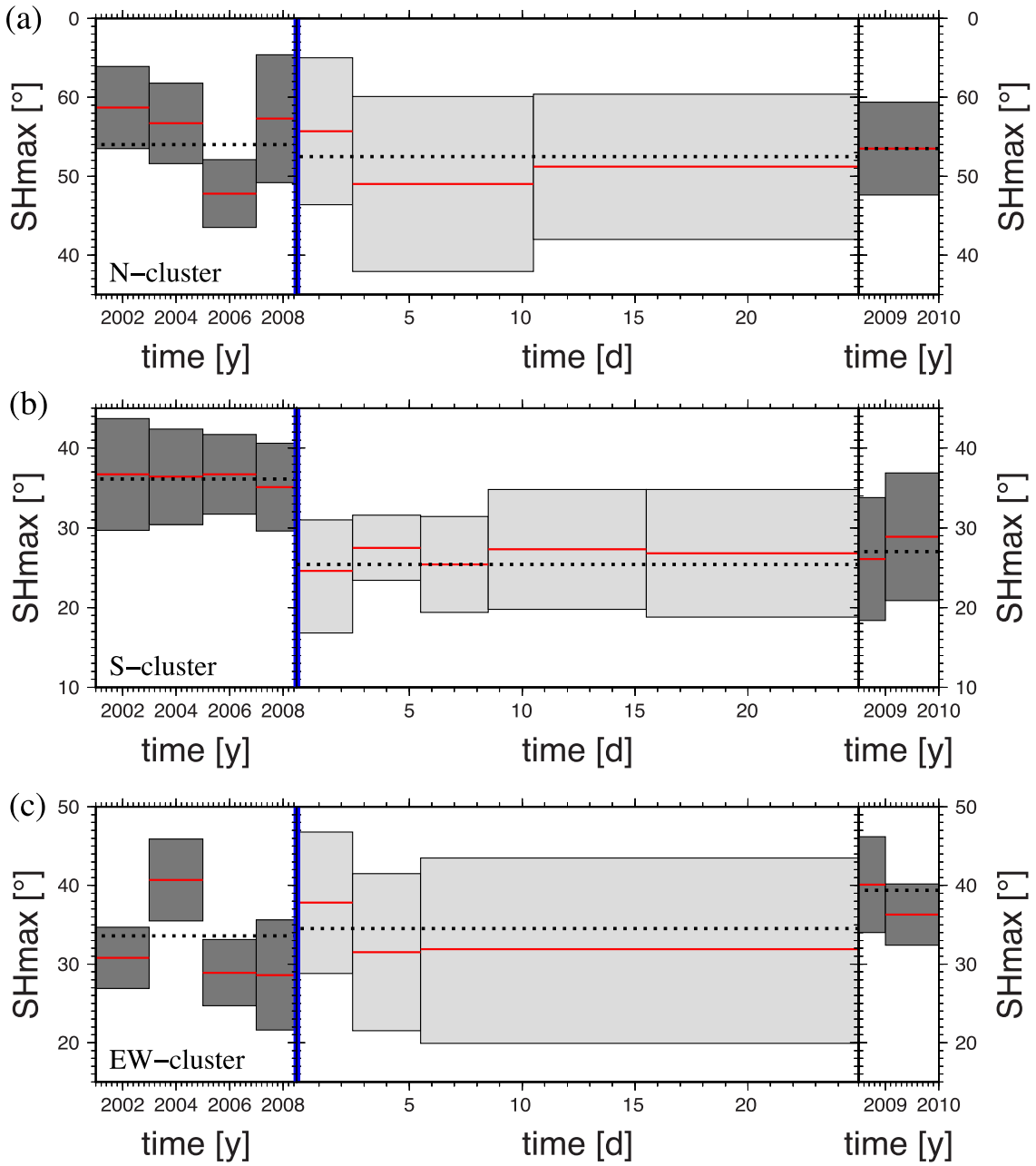


**Figure 5.** Maximum horizontal stress (SHmax) directions with respect to time for all three clusters [(a) northern, (b) southern and (c) east–west cluster]. Red lines mark the orientation of SHmax, boxes show the 95 per cent confidence level of each time interval (light grey for operation the time of the temporary network, dark grey for periods before and after). Dotted lines mark the SHmax direction for the whole time windows (2001 until main shocks, temporary network, after temporary network until end of 2009), residuals for inversions over the whole time windows are given in Table 3. The blue line gives the time of the main shocks on 2008 May 29.

Alternatively, $\Delta\tau$ can be calculated using fault dimension according to Lay & Wallace (1995) with

$$\Delta\tau = \frac{2}{\pi}\mu\left(\frac{\bar{D}}{W}\right) \tag{3}$$

Based on GPS and InSAR modeling, we use an average uniform slip $\bar{D}$ of 0.75–1.22 m, a fault width $W$ of 3–5 km and an average shear modulus $\mu$ of 40 GPa at 3 km depth, see Decriem *et al.* (2010). This approach indicates a stress drop of 4–10 MPa on the Kross fault.

Both these estimates of stress drop values are above the global average value of 3 MPa for interplate earthquakes (Stein & Wysession 2003) and slightly below the estimated stress drop of the 1987 Vatnafjöll earthquake in the eastern SISZ (12 MPa; Bjarnason (2015)). $\Delta\tau$ might be slightly overestimated using the circular crack model as it disregards the aspect ratio of the fault. In contrast, using uniform slip on the whole fault might lead to an underestimated stress drop in the region of most slip, that is, where we see strongest rotations of $\mathbf{S}_{\mathrm{H}}$.

Using the overlap of both estimates at 8–10 MPa, the obtained ratio of stress drop to maximum shear stress of $\Delta\tau/\tau = 0.5$ for the average coseismic rotation of $\mathbf{S}_{\mathrm{H}}$ thus implies a $\tau$ of 16–20 MPa. Regarding the uncertainties of the obtained $\Delta\tau/\tau$ and $\Delta\tau$, a conservative error estimate constrains $\tau$ in the range of 11–100 MPa using

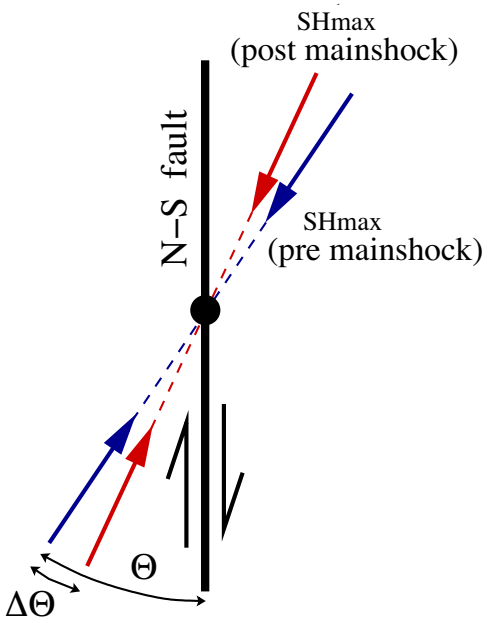


**Figure 6.** Geometry of the stress rotation on the north–south fault of the southern cluster. The blue arrow shows the pre-main shock and the red arrow the post-main shock orientation of SHmax.

95 per cent confidence, or 13–50 MPa when allowing for 68 per cent confidence levels.

In comparison, laboratory experiments show that the coefficient of friction in most rocks is around 0.6–0.85 (Byerlee 1978). Assuming rupture initiation at the depth of maximum slip at 4 km (Decriem *et al.* 2010), a density of 2.8 g cm$^{-3}$, friction coefficient of $\mu = 0.75$ and a pore fluid pressure of 40 per cent of the overburden pressure indicates that a shear stress in the order of around 40 MPa is needed to initiate the rupture process, according to eq. (7B) in Zoback & Townend (2001) for a strike-slip regime. This number is considerably larger than those that we found for the pre-main shock differential stress. The shear stress required to initiate rupture thus seems to be smaller than predicted by Byerlee's law. In other words, we find that the apparent strength of the Kross fault is lower than theoretically expected and also weaker than proposed by Bjarnason & Einarsson (1991) for the eastern SISZ.

Apparent fault weakness might be caused by several factors. These include potential weak gouges on the fault, dynamic weakening (Melosh 1996) or high pore fluid pressure as found for the 2000 earthquake in the central SISZ (Jónsson *et al.* 2003; Bonafede *et al.* 2007). Changes of pore fluid pressure can also have potential effects on the orientation of $\mathbf{S}_H$, as shown by Martínez-Garzón *et al.* (2013). Holt *et al.* (2013) observed a ratio of stress drop to background shear stress of 0.4 for the central segment of the 2010 $M_W$ 7.1 Darfield earthquake in New Zealand, if the apparent stress rotation was caused by the earthquake. This finding is close to our ratio of 0.5. However, due to a lack of seismicity prior to the main shock on that segment of the Darfield fault, the pre-event $\mathbf{S}_H$ direction is unknown. If $\mathbf{S}_H$ had not rotated due to the earthquake, but had the same direction prior and following the main shock, Holt *et al.* (2013) argue that a zone of high pore fluid pressure on the fault segment could account for this stress inhomogeneity. In our case the $\mathbf{S}_H$ direction on the Kross fault could be constrained prior to and following the main shocks, suggesting the rotation we estimate is primarily caused by coseismic slip on the Kross fault.

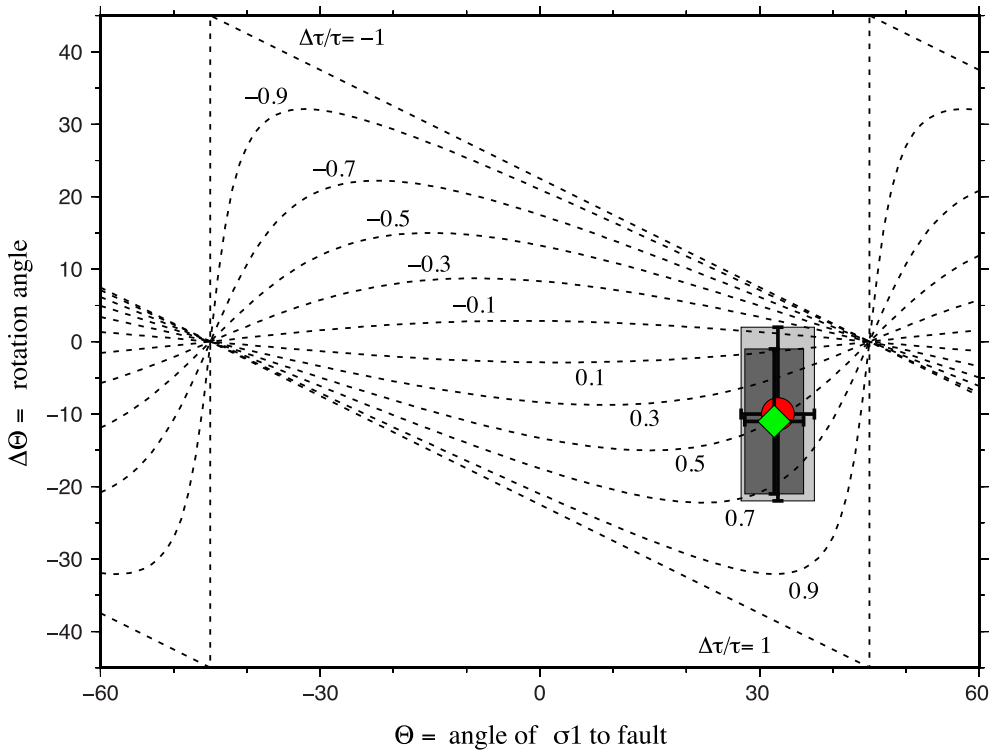


**Figure 7.** Rotation of the maximum horizontal stress direction ($\Delta\Theta$) as a function of the pre-event orientation of $\mathbf{S}_H$ ($\Theta$) with respect to the fault for selected $\Delta\tau/\tau$ (iso lines), according to Hardebeck & Hauksson (2001a). The green diamond and dark grey error box (95 per cent confidence) show the ratio of stress drop to the differential stress for the average rotation between the pre-event period and the first weeks of the aftershock sequence recorded with the temporary network, the red circle and light grey error box give the ratio between the last pre-event and the first aftershock interval.

The inferred weakness of the Kross fault might further be influenced by the fact that its failure was dynamically triggered by the first main shock on the adjacent Ingólfsfjall fault (Hreinsdóttir *et al.* 2009). This implies that the pre-earthquake shear stress was not sufficient to initiate a rupture on this fault, but required an external trigger. Eq. (1) represents the rotation of the uniform part of the stress field to the average stress drop on the scale of the fault length (Hardebeck & Hauksson 2001a). Our observations were made along the whole southern part of the Kross fault and results reflect average shear stress and fault strength on a length scale of kilometres. Locally higher shear stress magnitudes are well possible, for example, at crack tips and fault irregularities, and these could be sensitive to dynamic stress changes due to the first event.

In historic times, the SISZ has experienced earthquakes of magnitudes up to 7 in the central and eastern part of the zone, but rarely exceeding magnitude 6 in the western part (Stefánsson *et al.* 1993). Earthquake magnitudes in the western part are mainly limited by the thinner brittle crust close to the rift zone in western Iceland. The vicinity to the rift might further lower the frictional strength of the western SISZ faults and allow them to fail at lower differential stress compared to the eastern faults.

Summarizing all findings, we propose that around half of the background shear stress was released in the 2008 May main shock on the southern part of the Kross fault. Our results suggest a pre-main shock shear stress at 4 km depth on the Kross fault of around 20 MPa. However, evaluating the obtained uncertainties, the actual shear stress might be larger. Our ratio between stress drop and maximum shear stress is small compared to the 1992 Landers earthquake with $\Delta\tau/\tau$ ~0.65 (Hardebeck & Hauksson 2001a) and the 2011 Tohoku event, for which an almost complete stress drop was found (Hasegawa *et al.* 2011). The discrepancy between these results and our observations might be explained by the maturity of the faults. While the San Andreas fault and NE Japan subduction zone are well developed, faults in the SISZ are young and underdeveloped. Faults in the SISZ might in general be weaker close to the rift zone in the western part, compared to the central and eastern part, and thus allowing rupture at lower ambient differential stress than theoretically expected.

In contrast to the S-cluster, no comparable rotations were found for the N- and EW-clusters. In general, larger uncertainties of the stress directions are found in these two clusters, compared to the S-cluster. This might indicate that the stress fields in the N- and EW-clusters are more heterogeneous and different faults with different orientations and slip directions might have been activated in the N- and EW-clusters.

The N-cluster extends into the eastern part of Hengill volcano. Hengill marks a triple junction between the Eurasian and Northern American plates, as well as the border to the Hreppar microplate in central Iceland (Einarsson 1991). Hengill is located at the southern end of the Western Volcanic Zone, with similar NE–SW striking normal faults outlining the fissure swarm as observed on the Reykjanes peninsula. The normal faulting stress regime found in the N-cluster prior to the 2008 activity is thus likely to reflect higher seismicity rates on the normal faults within the rift zone, and lower rates of seismicity on the N-S strike-slip faults of the SISZ. This assumption is supported by the depth distribution of the events. Pre-main shock earthquakes in the N-cluster are located at shallow depths of around 5 km. This fits observations on the adjacent Reykjanes peninsula, where seismic activity occurs in comparable local normal and strike-slip faulting regimes (Einarsson 1991; Keiding *et al.* 2009). In contrast, earthquakes in the S- and EW-clusters mainly occur between 4 and 8 km depth with almost pure strike-slip faults. The apparent stress rotation in the N-cluster from normal faulting to strike-slip faulting is consequently interpreted to reflect stress heterogeneities and activity on different adjacent fault systems within the N-cluster, which is further suggested by the slight change in location between pre- and aftershock activity in the N-cluster.

Hengill experienced a period of unrest between 1993 and 1999, suggestively driven by a magma intrusion. Inflation rates of 2 cm $yr^{-1}$ were observed during that time, with a centre of uplift about 5 km NW of the Kross fault (Sigmundsson *et al.* 1997; Feigl *et al.* 2000). This might have increased NW-SE oriented stress on the N-S orientated faults and potentially had influence on the timing of the 2008 Ölfus earthquakes. Decreased normal stress on the N-S faults due to subsidence in Hengill from around the year 2000 possibly unlocked the system and eventually facilitated the main shocks. However, this hypothesis requires careful analysis and thus remains speculative.

As geodetic measurements did not indicate significant slip in the EW-cluster, the absence of significant stress changes is not unexpected. Decriem *et al.* (2010) modeled an increase of Coulomb failure stress in this region due to the main shock on the Kross fault, leading to static triggering of seismic activity. The activation of this E-W elongated zone has repeatedly been observed following previous SISZ earthquakes and interpreted as right-lateral motion on a series of N-S oriented faults (Rögnvaldsson *et al.* 1998a,b; Vogfjörd *et al.* 2005). A hint of clockwise rotation between the last pre- and first post-main shock time interval, as well as for the following 1.5 yr is obscured by large uncertainty levels. Clockwise rotation to a $\mathbf{S}_{\mathrm{H}}$ direction closer to 45° implies a stress load on these faults, as expected by Decriem *et al.* (2010). This can, however, not be resolved with our data.

## 5 CONCLUSIONS

The 2008 May earthquakes in the western SISZ caused a localized counter-clockwise rotation of the maximum horizontal stress direction $\mathbf{S}_{\mathrm{H}}$ of 11 ± 10° on the southern part of the Kross fault (S-cluster), from 36 ± 5° to 25 ± 5°. The stress drop on this fault segment is estimated to have been 8–10 MPa. The ratio between the stress drop and the ambient maximum shear stress is found to be 0.5, corresponding to a maximum shear stress of 16–20 MPa, which is much lower than the theoretically expected shear stress of around 40 MPa. The apparent weakness of the Kross fault is suggested to be caused by fault properties, high pore fluid pressures and possibly weaker faults close to the western rift zone relative to the eastern part of the SISZ, and might further be influenced by the stress increase due to the initial rupture on the Ingólfsfjall fault.

The observed flip from normal faulting prior to and strike-slip faulting following the main shocks on the northern end of the Kross fault most likely reflects a change from dominant activity on the NE–SW fissures of Hengill volcano to the N-S faults of the SISZ as a response to the two main shocks. This perturbation is likely linked to local stress heterogeneities or activation of adjacent, but different faults, rather than a response to the slip on the Kross fault.

The absence of any obvious stress rotation, as well as the observation of large uncertainties of the stress direction and irregular jumps in the E-W elongated aftershock zone west of the main ruptures implies local stress heterogeneities rather than stress changes linked to significant slip in this region.

## ACKNOWLEDGEMENTS

We thank the Icelandic Research Fund (RANNÍS) for financial support. The temporary SISZ2008 network was installed and maintained by Ólafur Guðmundsson and Bryndís Brandsdóttir, with the help from Ingi Þ. Bjarnason, Magnús Pálsson, Rögnvaldur Magnússon and Indíana Ingólfsdóttir. The SIL-monitoring group of the IMO located all events recorded by the permanent network. Páll Einarsson provided surface fault location data. BSc students Hanna Blanck and Jakob Smári Ævarsson helped with the manual picking of the joint data set. Comments from John Townend and an anonymous reviewer improved the manuscript. The Generic Mapping Tools (GMT) (Wessel & Smith 1998) were used to produce the figures.

## REFERENCES

Árnadóttir, T., Hreinsdóttir, S., Gudmundsson, G., Einarsson, P., Heinert, M. & Völkssen, C., 2001. Crustal deformation measured by GPS in the South Iceland Seismic Zone due to two large earthquakes in June 2000, *Geophys. Res. Lett.,* **28,** 4031–4033.

Árnadóttir, T., Jónsson, S., Pedersen, R. & Gudmundsson, G., 2003. Coulomb stress changes in the South Iceland Seismic Zone due to two large earthquakes in June 2000, *Geophys. Res. Lett.,* **30**(5), 1205, doi: 10.1029/2002GL016495.

Árnadóttir, T., Jiang, W., Feigl, K., Geirsson, H. & Sturkell, E., 2006. Kinematic models of plate boundary deformation in southwest Iceland derived from GPS observations, *J. geophys. Res.,* **111,** B03302, doi:10.1029/2005JB003935.

Bjarnason, I., 2015. The 1973-1996 Earthquake sequence in Bárðarbunga volcano. Seismic activity leading up to eruptions in northwestern Vatnajökull area, *Jökull,* **64,** 61–82.

Bjarnason, I. & Einarsson, P., 1991. Source mechanism of the 1987 Vatnafjöll earthquake in South Iceland, *J. geophys. Res.,* **96,** 4313–4324.

Bjarnason, I., Cowie, P., Anders, M., Seeber, N. & Scholz, C., 1993. The 1912 Iceland earthquake rupture: growth and development of a nascent transform system, *Bull. seism. Soc. Am.,* **83,** 416–435.

Bödvarsson, R., Rögnvaldsson, S. & Slunga, R., 1999. The SIL data acquisition system—at present and beyond the year 2000, *Phys. Earth planet. Inter.,* **113**(1), L11309, doi:10.1016/S0031-9201(99)00032-1.

Bonafede, M., Ferrari, C., Maccaferri, F. & Stefánsson, R., 2007. On the preparatory processes of the M6.6 earthquake of June 17th, 2000, in Iceland, *Geophys. Res. Lett.,* **34,** L24305, doi:10.1029/2007GL031391.

Brandsdóttir, B., Parsons, M., White, R., Gudmundsson, O., Drew, J. & Thorbjarnadóttir, B., 2010. The May 29th 2008 earthquake aftershock sequence within the South Iceland Seismic Zone: fault locations and source parameters of aftershocks, *Jökull,* **60,** 23–46.

Brune, J., 1970. Tectonic stress and spectra of seismic shear waves from earthquakes, *J. geophys. Res.,* **75,** 4997–5009.

Brune, J., 1971. Correction of: tectonic stress and spectra of seismic shear waves from earthquakes, *J. geophys. Res.,* **76,** 5002, doi:10.1029/JB075i026p04997.

Byerlee, J., 1978. Friction of rock, *Pure appl. Geophys.,* **116,** 615–626.

Decriem, J. *et al.*, 2010. The 2008 May 29 earthquake doublet in SW Iceland, *Geophys. J. Int.,* **181,** 1128–1146.

DeMets, C., Gordon, R. & Argus, D., 2010. Geologically current plate motions, *Geophys. J. Int.,* **181,** 1–80.

Einarsson, P., 1991. Earthquakes and present-day tectonism in Iceland, *Tectonophysics,* **189,** 261–279.

Einarsson, P., 2010. Mapping of Holocene surface ruptures in the South Iceland Seismic Zone, *Jökull,* **60,** 117–134.

Einarsson, P. & Björnsson, S., 1979. Earthquakes in Iceland (Jardskjálftar á Íslandi), *Jökull,* **29,** 37–43.

Einarsson, P. & Sæmundsson, K., 1987. Earthquake epicenters 1982–1985 and volcanic systems in Iceland. Map accompanying Festschrift for Th. Sigurgeirsson, in *Í Hlutarins Edli,* ed. Sigfusson, T., Menningarsjódur, Reykjavík, Iceland.

Einarsson, P., Björnsson, S., Foulger, G., Stefánsson, R. & Skaftadóttir, T., 1981. Seismicity pattern in the South Iceland Seismic Zone, *Earthq. Predict., American Geophys. Union,* Washington, DC, **4,** 141–151.

Feigl, K., Gasperi, J., Sigmundsson, F. & Rigo, A., 2000. Crustal deformation near Hengill volcano, Iceland 1993-1998: coupling between magmatic activity and faulting inferred from elastic modeling of satellite radar interferograms, *J. geophys. Res.,* **105,** 655–670.

Gephart, J. & Forsyth, D., 1984. An improved method for determining the regional stress tensor using earthquake focal mechanism data: application to the San Fernando earthquake sequence, *J. geophys. Res.,* **89,** 9305–9320.

Hardebeck, J., 2012. Coseismic and postseismic stress rotations due to great subduction zone earthquakes, *Geophys. Res. Lett.,* **39,** L21313, doi:10.1029/2012GL053438.

Hardebeck, J. & Hauksson, E., 2001a. Crustal stress field in southern California and its implications for fault mechanisms, *J. geophys. Res.,* **106**(10), 21859–21882.

Hardebeck, J. & Hauksson, E., 2001b. Stress orientations obtained from earthquake focal mechanisms: what are appropriate uncertainty estimates?, *Bull. seism. Soc. Am.,* **91,** 250–262.

Harris, R. & Simpson, R., 1992. Changes in static stress on southern California faults after the 1992 Landers Earthquake, *Nature,* **360,** 251–254.

Hasegawa, A., Yoshida, K. & Okada, T., 2011. Nearly complete stress drop in the 2011 $M_W$ 9.0 off the Pacific coast of Tohoku Earthquake, *Earth Planet Space,* **63,** 703–707.

Hauksson, E., 1994. State of stress from focal mechanisms before and after the 1992 Landers earthquake sequence, *Bull. seism. Soc. Am.,* **84**(3), 917–934.

Havskov, J. & Ottemöller, L., 2008. *SEISAN–The Earthquake Analysis Software, version 8.2.1*, Institute of Solid Earth Physics, University of Bergen, Norway.

Hjaltadóttir, S., 2009. Use of relatively located microearthquakes to map fault patterns and estimate the thickness of the brittle crust in Southwest Iceland, *Master's thesis,* Faculty of Earth Sciences, University of Iceland, Reykjavík, Iceland.

Hjaltadóttir, S. & Vogfjörd, K., 2005. Subsurface fault mapping in Southwest Iceland by relative location of aftershocks of the June 2000 earthquakes. Rep. VÍ-ES-01, 18, Icelandic Meteorol. Off.

Holt, R., Savage, M., Townend, J., Syracuse, E. & Thurber, C., 2013. Crustal stress and fault strength in the Centerbury Plains, New Zealand, *Earth planet. Sci. Lett.,* **383,** 173–181.

Hreinsdóttir, S., Árnadóttir, T., Decriem, J., Geirsson, H., Tryggvason, A., Bennet, R. & LaFemina, P., 2009. A complex earthquake sequence captured by the continuous GPS network in SW Iceland, *Geophys. Res. Lett.,* **36,** L12309, doi:10.1029/2009GL038391.

Ickrath, M., Bohnhoff, M., Bulut, F. & Dresen, G., 2013. Stress rotation and recovery in conjunction with the 1999 Izmit $M_W$7.4 earthquake, *Geophys. J. Int.,* **196,** 951–956.

Jónsson, S., Segall, P., Pedersen, R. & Björnsson, G., 2003. Post-earthquake ground movements correlated to pore-pressure transients, *Nature,* **424,** 179–183.

Kagan, Y., 2005. Double-couple earthquake focal mechanism: random rotation and display, *Geophys. J. Int.,* **163**(3), 1065–1072.

Keiding, M., Lund, B. & Árnadóttir, T., 2009. Earthquakes, stress and strain along an oblique divergent plate boundary: Reykjanes Peninsula, southwest Iceland, *J. geophys. Res.,* **114,** B09306, doi:10.1029/2008JB006253.

Lay, T. & Wallace, T., 1995. *Modern Global Seismology,* vol. 58, Academic Press.

Lund, B. & Slunga, R., 1999. Stress tensor inversion using detailed microearthquake information and stability constraints: application to Ölfus in southwest Iceland, *Geophys. Res. Lett.,* **104,** 14.947–14.964.

Lund, B. & Townend, J., 2007. Calculating horizontal stress orientations with full or partial knowledge of the tectonic stress tensor, *Geophys. J. Int.,* **170,** 1328–1335.

Martínez-Garzón, P., Bohnhoff, M., Kwiatek, G. & Dresen, G., 2013. Stress tensor changes related to fluid-injection at the Geysers geothermal field, California, *Geophys. Res. Lett.,* **40,** 2596–2601.

Melosh, H., 1996. Dynamical weakening of faults by acoustic fluidization, *Nature,* **379,** 601–606.

Michael, A., 1984. Determination of stress from slip data: faults and folds, *J. geophys. Res.,* **89,** 11517–11526.

Michael, A., 1987. Stress rotation during coalinga aftershock sequence, *J. geophys. Res.,* **92,** 7963–7979.

Pedersen, R., Jónsson, S., Árnadóttir, T., Sigmundsson, F. & Feigl, K.L., 2003. Fault slip distribution of two $M_w$ 6.5 earthquakes in South Iceland estimated from joint inversion of InSAR and GPS measurements, *Earth planet. Sci. Lett.,* **213,** 487–502.

Reinhardt, J., 2007. Inversion for local stress field inhomogenities, *PhD thesis,* University of Hamburg, Germany, ZMAW library.

Rögnvaldsson, S., Gudmundsson, G., Ágústsson, K., Jakobsdóttir, S., Slunga, R. & Stefánsson, R., 1998a. Overview of the 1993-1996 seismicity near Hengill. Tech. Rep. VÍ-R98006, Icelandic Meteorol. Off., Reykjavík, Iceland.

Rögnvaldsson, S. & Slunga, R., 1993. Routine fault plane solutions for local networks: a test with synthetic data, *Bull. seism. Soc. Am.,* **83**(4), 1232–1247.

Rögnvaldsson, S. *et al.*, 1998b. Skjálftahrina í Ölfusi í nóvember 1998. Tech. Rep. VÍ-G98046-JA09, Icelandic Meteorol. Off., Reykjavík, Iceland, (in Icelandic).

Sigmundsson, F., Einarsson, P., Rögnvaldsson, S., Foulger, G., Hodgkinson, K. & Thorbergsson, G., 1997. The 1994-1995 seismicity and deformation at the Hengill triple junction, Iceland: triggering of earthquakes by minor magma injection in a zone of horizontal shear stress, *J. geophys. Res.,* **102,** 15151–15161.

Slunga, R., 1981. Earthquake source mechanism determination by use of body-wave amplitudes—an application to Swedish earthquakes, *Bull. seism. Soc. Am.,* **71,** 25–35.

Snoke, J., Munsey, J., Teague, A. & Bollinger, G., 1984. A program for focal mechanism determination by combined use of polarity and SV-P amplitude ratio data, *Earthq. Notes,* **55,** 3–15.

Stefánsson, R. *et al.*, 1993. Earthquake prediction research in the South Iceland Seismic Zone and the SIL project, *Bull. seism. Soc. Am.,* **83,** 696–716.

Stein, S. & Wysession, M., 2003. *An Introduction to Seismology, Earthquakes and Earth Structure,* Blackwell Publishing Ltd.

Townend, J. & Zoback, M., 2001. Implications of earthquake focal mechanisms for the frictional strength of the San Andreas fault system, *Geol. Soc. Lond., Spec. Publ.,* **186,** 13–21.

Vogfjörd, K.S., Hjaltadóttir, S. & Slunga, R., 2005. Volcano-tectonic interaction in the Hengill region, Iceland during 1993–1998, in *Geophys. Res. Abs.,* EGU05-J-09947, vol. 7, European Geosciences Union.

Wessel, P. & Smith, W., 1998. New, improved version of generic mapping tools released, *EOS, Trans. Am. geophys. Un.,* **79,** 579, doi:10.1029/2008JB006253.

Wyss, M. & Stefánsson, R., 2006. Nucleation points of recent mainshocks in Southern Iceland, mapped by b-values, *Bull. seism. Soc. Am.,* **96**(2), 599–608.

Zoback, M. & Townend, J., 2001. Implications of hydrostatic pore pressure and high crustal strength for the deformation of intraplate lithosphere, *Tectonophysics,* **336,** 19–30.